scientific reports

Check for updates

OPEN

Fabrication, defect chemistry and microstructure of Mn-doped UO_2

H. Smith[1], L. T. Townsend[1], R. Mohun[1], J. F. W. Mosselmans[2], K. Kvashnina[3,4], Neil C. Hyatt[5,6] & C. L. Corkhill[1,6]✉

Mn-doped UO_2 is under consideration for use as an accident tolerant nuclear fuel. We detail the synthesis of Mn-doped UO_2 prepared via a wet co-precipitation method, which was refined to improve the yield of incorporated Mn. To verify the Mn-doped UO_2 defect chemistry, X-ray absorption spectroscopy at the Mn K-edge was performed, in addition to X-ray diffraction, Raman spectroscopy and high-energy resolved fluorescence detection X-ray absorption near edge spectroscopy at the U M_4-edge. It was established that Mn^{2+} directly substitutes for U^{4+} in the UO_2 lattice, accompanied by oxygen vacancy (O_v) charge compensation. In contrast to other divalent-element doped UO_2 materials, compelling evidence for U^{5+} in a charge compensating role was not found. This work furthers understanding of the structure and crystal chemistry of Mn-doped UO_2, which could show potential advantages as a novel efficient advanced nuclear fuel.

In so-called advanced nuclear fuels, it has been shown that by adding small amounts of Cr-dopant to the UO_2 matrix the grain size is increased, resulting in a longer pathway for fission gasses to migrate and escape the fuel matrix, thus reducing pellet swelling during reactor operations. Other favourable properties are promoted upon Cr doping, including improved plasticity and reduced pellet-cladding interactions, all of which reduce the risk of fuel failure[1–5]. The introduction of Mn as a dopant in UO_2 fuels has been hypothesised to offer an improved alternative to commercially available Cr-doped UO_2 fuel[6], warranting further study of the crystal chemistry of Mn-doped UO_2.

Atomistic modelling of the Mn-doped UO_2 crystal lattice and defect formation during heat treatment suggested that grain growth is enhanced by the formation of U vacancy defects (U_v) that aid diffusion during the sintering process[7]. These defects are predicted to increase in concentration with the presence of dopants when compared to undoped UO_2. Through atomistic modelling, the U_v concentration was shown to be up to five times greater in Mn-doped UO_2 than Cr-doped UO_2, strongly suggesting that Mn-doped UO_2 should exhibit larger grains and, therefore, enhanced in-reactor properties with regards to fission gas migration. Experimental investigation of the synthesis of Mn-doped UO_2 via a sol–gel method found grain size enhancement of up to 80 µm in samples when compared to UO_2, with a measured Mn content of 490 ppm. In comparison, grains of ~ 50 µm were achieved in 350 ppm Cr-doped UO_2 when both were sintered at 1700 °C for 6 h under a reducing Ar-4%H_2 atmosphere[8].

Grain size growth has also been postulated to be the result of the formation of a liquid phase in Mn-doped UO_2, where MnO powder was dry mixed with an additional dopant, Al_2O_3, to form a 1000 ppm Mn/Al-doped UO_2[9]. When sintered at 1860 °C, which is close to the melting temperature of MnO (1945 °C), a maximum grain size of ~ 50 µm was achieved, attributed to a MnO-Al_2O_3 binary liquid phase. The mechanism of grain growth in Mn-doped UO_2 is, therefore, unclear and further investigation into dopant concentration and solubility of Mn in the UO_2 lattice is warranted to optimise fuel fabrication routes.

Additionally, post-operation of a nuclear reactor, the safe storage and disposal of spent fuel is dependent on the long-term durability of the UO_2 matrix, most prominently when exposed to geological disposal conditions[10,11]. Matrix oxidation converts the relatively insoluble $U^{(4+)}O_2$ to soluble $U^{(6+)}O_2^{2+}$ and, as such, under

[1]Department of Materials Science and Engineering, The University of Sheffield, Sheffield, UK. [2]Diamond Light Source, Harwell Science and Innovation Campus, Didcot, UK. [3]Institute of Resource Ecology, Helmholtz-Zentrum Dresden-Rossendorf (HZDR), P.O. Box 510119, 01314 Dresden, Germany. [4]The Rossendorf Beamline at ESRF, The European Synchrotron, CS40220, 38043 Grenoble Cedex 9, France. [5]School of Mechanical and Materials Engineering, Washington State University, Pullman, WA 99164, USA. [6]School of Earth Science, The University of Bristol, Bristol, UK. ✉email: c.corkhill@bristol.ac.uk

geological disposal conditions, may result in radionuclide release into groundwater. Therefore, any alteration to UO_2 that may result in oxidation will undoubtedly influence dissolution behaviour and so understanding how dopants affect these properties is crucial to ensuring safe disposal of radioactive waste. For example, it was recently found that the addition of Cr to UO_2, reduced the dissolution rate of U, through a galvanic coupling effect between Cr^{2+} and U^{6+} [12]. A thorough understanding of the crystal chemistry of Mn-doped UO_2 in comparison to undoped UO_2, including an investigation of defect formation, is thus required to fully underpin predictions of spent fuel dissolution behaviour over the geological disposal period (100,000 + years).

While dry-synthesis and sol–gel methods have been demonstrated for the synthesis of Mn-doped UO_2, this work improves upon these processes using an alternative wet chemical co-precipitation synthesis route. To aid a detailed study of the local structure of Mn in UO_2, the samples were sintered in a consistent reducing environment. Analysis of Mn-doped UO_2, prior to, and after sintering, was performed by X-ray absorption spectroscopy (XAS), X-ray diffraction (XRD), and Raman spectroscopy. The effects of sintering in a reducing environment on the final microstructure and crystal chemistry is also discussed, completing an in-depth experimental study of Mn-doped UO_2 crystal chemistry and providing a key foundation for future investigations of the use of Mn-doped UO_2 as an advanced nuclear fuel.

Results & discussion

Development of Mn-doped UO_2 synthesis and fabrication method

A nitrate co-precipitation method was developed to prepare Mn-doped UO_2 with an initial target concentration of 1200 ppm Mn, in which nitrates of Mn ($Mn(NO_3)_3{\cdot}4H_2O$) and U ($UO_2(NO_3)_2{\cdot}6H_2O$) were used. Concentrated NH_4OH was added to this mixture in 0.1 mL instalments until a pH of 7, 9, 10 or 11 was reached and precipitation of a mixed compound was achieved. Analysis of the supernatants via Inductively Coupled Plasma-Optical Emission Spectroscopy indicated the success of co-precipitation of Mn for each pH, where ~ 99.00 ± 1.00% U was precipitated for all pH values. The Mn incorporation in the resulting solid upon precipitation varied, with 84.98 ± 0.01%, 99.96 ± 0.03%, 99.80 ± 0.03% and 99.9 ± 0.6% Mn incorporated for pH 7, 9, 10 and 11, respectively (Fig. 1a). This indicates that a pH of ≥ 9 is required to fully incorporate Mn within co-precipitated product. Consideration of both the supernatant analysis and a complete nitric acid digest of the solids confirmed that the optimal synthesis was achieved at pH 10 and, as such, the remainder of the samples discussed herein were fabricated using material precipitated at pH 10.

An optimal calcination temperature was determined by Thermogravimetric analysis of the precipitated precursor material (Fig. 1b), where mass losses due to the removal of water (100–190 °C)[13], U/Mn and ammonia nitrate from synthesis (200–300 °C)[14,15], and the decomposition of nitrate oxides formed during heating (300–525 °C)[15], occurred up to a temperature of ~ 600 °C. The DTA curve shows endothermic peaks, A and C, relating to water loss and decomposition of nitrate oxides, respectively, and an exothermic peak, B, attributed to the formation nitrate oxides during heating. A calcination temperature of 750 °C was selected and conversion from precursor material (identified as $3UO_3{\cdot}2NH_3{\cdot}4H_2O$) to UO_2 after heat treatment for 4 h under a reducing atmosphere (95% N_2/5% H_2) was confirmed via XRD of the calcined powder (Fig. 1c).

Crystal chemistry of Mn-doped UO_2

Mn K-edge X-ray absorption near edge spectroscopy (XANES) analysis of Mn-doped UO_2 showed a unique coordination environment when compared to standards of known speciation (Fig. 2a). Of the different Mn standards measured, the E_0 position (white line, taken from the peak of the first derivative) of Mn-doped UO_2 (6551 ± 0.3 eV) was closest to that of the Mn^{2+} standards (6550–6552 ± 0.6 eV) (Table 1); however, spectrally, each Mn^{2+} standard was clearly different to the samples, suggesting that Mn in UO_2 does not possess a local environment similar to those of the Mn standards.

Analysis of the pre-edge feature in the Mn K-edge XANES (Fig. 2b and Supplementary Material Fig. 1) can be used to probe the local symmetry environment[16,17]. This pre-edge feature arises from the forbidden *1s* to *3d* electronic transition and becomes more intense when there is stronger mixing of the *d* and *p* orbitals resulting from a lack of local symmetry in the Mn environment[18]. Here, the centroid position and integrated area of the pre-edge feature were similar for all Mn-doped UO_2 samples (6540.42–6540.64 eV and 0.0490–0.0994, respectively) (Fig. 2b and Table 1). These values are in accordance with those determined for standards that contain Mn^{2+} in an octahedral local symmetry environment (6540.36–6540.83 eV and 0.055–0.285 for the centroid position and integrated area, respectively). The values for Mn-doped UO_2 were also in agreement with literature values for $(Mn^{2+},Fe)_3Al_2Si_3O_{12}$ (6540.66 eV, 0.0745)[17], which exhibits a cubic Mn local environment; however, the same study reports similar values for octahedrally-coordinated $Mn^{2+}O$ (6540.62 eV, 0.0745). This highlights that differentiation in the local symmetry of Mn^{2+} by pre-edge analysis is not simple and that additional Extended X-ray Absorption Fine Structure (EXAFS) analysis is required to confirm the coordination environment.

Since there were no changes in the XANES spectral features with increasing Mn content, nor between calcined oxide powder and sintered samples (Fig. 2), the 1200 ppm and 2400 ppm Mn-doped UO_2 calcined powder samples were selected as representative of the local structure of Mn in UO_2 for EXAFS fitting of the Mn K-edge. In agreement with the models of Mn-doping in UO_2 developed by Cooper et al.[7], the fitted data for both concentrations (Fig. 3, Table 2; corresponding data for the sintered material is given in Supplementary Material Fig. 2), indicated that the first O nearest neighbour environment of Mn is split between 6 O atoms at 2.27–2.29 ± 0.01 Å and 2 O atoms at 2.55–2.57 ± 0.03 Å in an eightfold coordination environment, consistent with direct substitution of Mn onto the U^{4+} site, or onto an interstitial site[7]. Slight contraction in the first Mn–O distance, when compared to 2.36 ± 0.02 Å U–O distance, is to be expected if Mn is substituted onto the U^{4+} site, due to the smaller cation size of Mn^{2+} (0.96 Å) compared to U^{4+} (1.00 Å). This contraction also creates a small

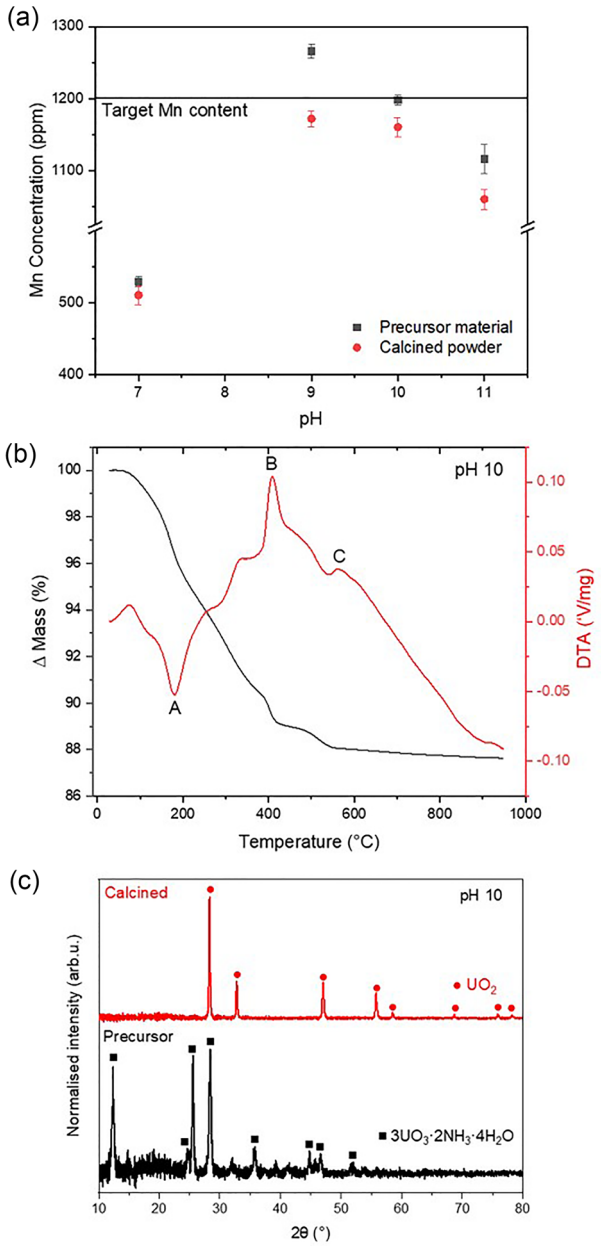

Figure 1. Initial investigation of an optimal synthesis and fabrication route for Mn-doped UO_2. (**a**) Complete digest of target 1200 ppm Mn-doped UO_2 synthesised at pH 7, 9, 10 and 11; (**b**) Thermogravimetric analysis of precursor material synthesised at pH 10 and; (**c**) X-ray diffraction patterns of precursor and calcined material (pH 10).

amount of distortion in the local Mn environment, which is likely the reason for the first coordination shell splitting into two different O distances.

Substitution of Mn^{2+} on the U^{4+} lattice site is further supported by a decrease in the lattice parameter with increasing Mn content, consistent with Vegard's Law (Fig. 4). Both calcined powder and sintered samples maintained the fluorite crystal structure of UO_2 (Supplementary Material Fig. 3). Beyond the first coordination shell, a further 5 U atoms were fit at distance of 3.78 ± 0.01 Å (Table 2). The decreased coordination from the expected 12 U atoms at 3.85 ± 0.06 Å in crystalline UO_2 may be attributed to a combination of lattice distortion from Mn-doping and of the limited data range available (2–10.5 $Å^{-1}$). The combination of these two factors makes delineation of the distorted U-U backscatterers challenging; extension of the data range, not practically possible in this experiment due to the low Mn concentrations within a highly absorbing UO_2 matrix, could resolve this.

The bond valence sum (BVS) was calculated and used to indicate the oxidation state. Values of 1.80 and 1.88 were calculated for the 1200 ppm and 2400 ppm Mn-doped UO_2 samples, respectively, supporting the presence of Mn^{2+} (Table 2). This is in agreement with recently published studies of the coordination of Cr doped in the UO_2 structure, which was found as Cr^{2+} in calcined material[19].

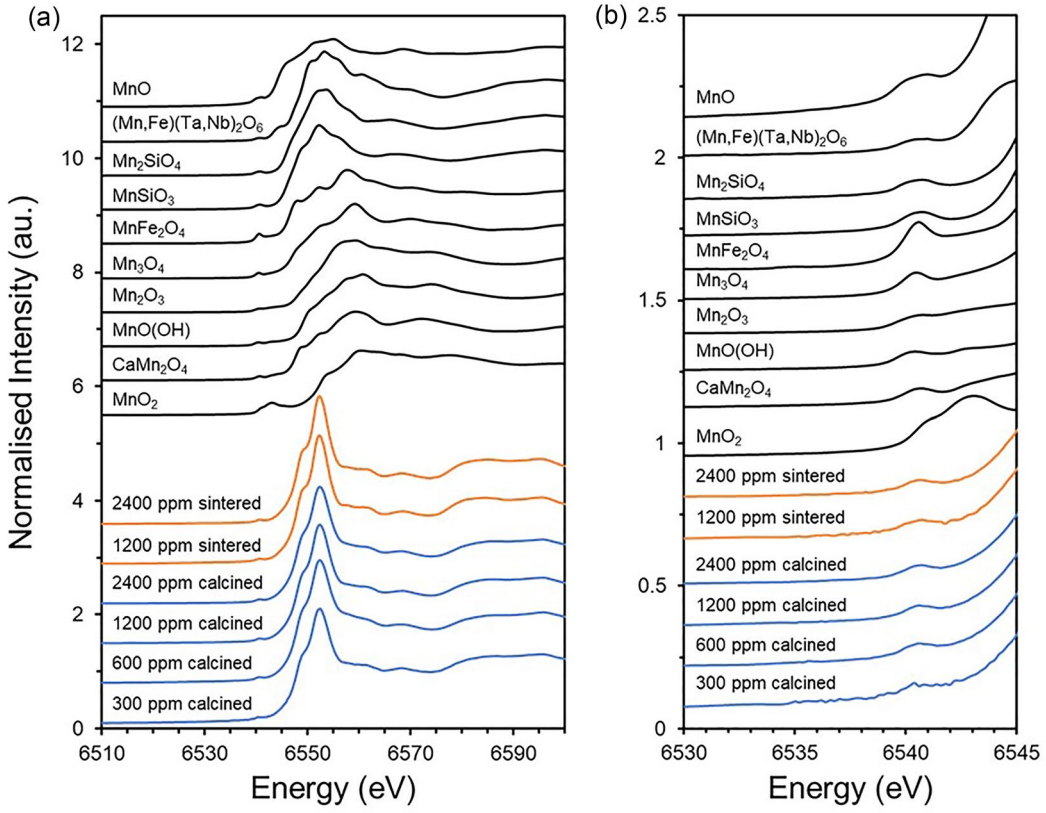

Figure 2. Mn K-edge XANES spectra of Mn doped UO_2 compared to known standards. (**a**) complete spectra and; (**b**) pre-edge region. Standards are depicted in black, with calcined samples in blue and sintered samples in orange.

Sample/Standard	Valence state	Mn environment	E_0 (white line) position (eV, ± 0.6)	Pre-edge centroid position (eV, ± 0.6)	Pre-edge integrated area (± 0.03)
300 ppm Mn (Calcined)			6551	6540	0.049
600 ppm Mn (Calcined)			6551	6540	0.099
1200 ppm Mn (Calcined)			6551	6540	0.072
1200 ppm Mn (Sintered)	1.80[a]	Distorted cubic[b]	6551	6540	0.078
2400 ppm Mn (Calcined)			6551	6540	0.064
2400 ppm Mn (Sintered)	1.88[a]	Distorted cubic[b]	6551	6540	0.072
$(Mn,Fe)(Ta,Nb)_2O_6$	2	O_h	6552	6540	0.055
Mn_2SiO_4	2	O_h	6550	6540	0.155
$MnSiO_3$	2	O_h[c]	6551	6540	0.186
MnO	2	O_h	6550	6540	0.286
$MnFe_2O_4$	2	T_d	6556	6541	0.481
Mn_3O_4	2/3	O_h /T_d	6557	6541	0.112
Mn_2O_3	3	O_h	6554	6541	0.231
MnO(OH)	3	O_h	6556	6541	0.148
$CaMn_2O_4$	3	O_h	6555	6541	0.010
MnO_2	4	O_h	6558	6542	0.510

Table 1. XANES analysis for Mn-doped UO_2 samples and Mn standards. (O_h) is octahedral and (T_d) is tetrahedral local symmetry environment. [a]Calculated bond valence sum from EXAFS model (Table 2); [b]Determined from EXAFS models (Table 2); [c] distorted[16].

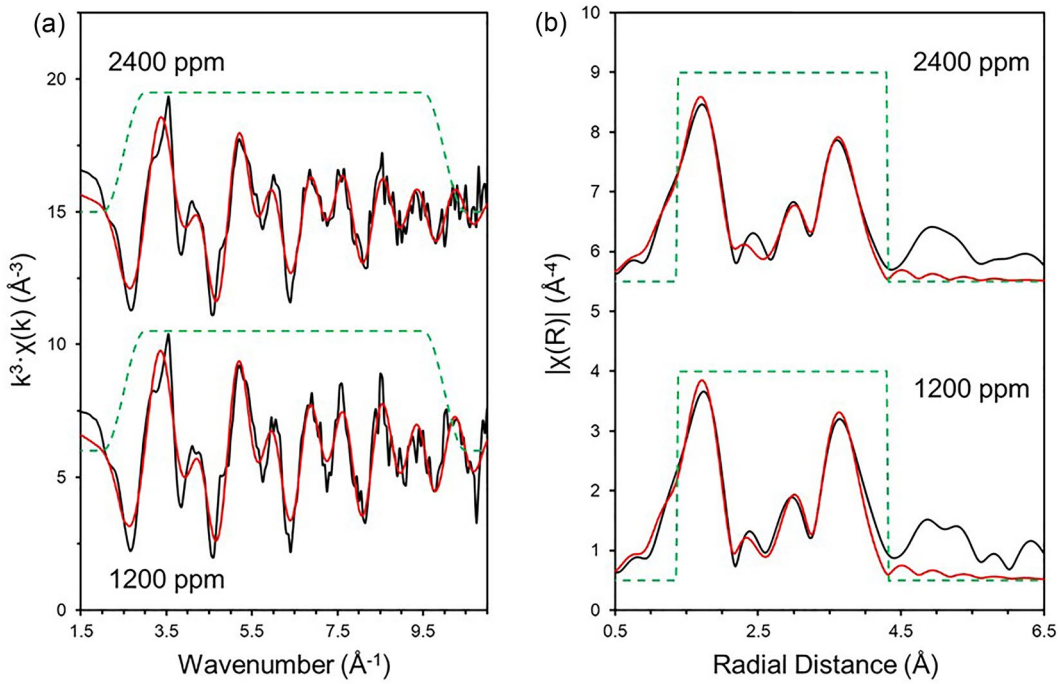

Figure 3. Mn K-edge spectra (black lines) and EXAFS model fits (red lines) for nominally doped 1200 ppm and 2400 ppm Mn calcined powder samples. (**a**) k^3-weighted EXAFS; and (**b**) Fourier transform of the k^3-weighted EXAFS, using a Hanning window function.

	UO_2 + 1200 ppm Mn (Calcined oxide powder)	UO_2 + 2400 ppm Mn (Calcined oxide powder)
S_0^2	1.0	1.0
ΔE_o	− 0.8 (1)	− 0.9 (6)
N (Mn-O1)	6	6
R_{eff} (Mn-O1)	2.37	2.37
R(Mn-O1)	2.29 (1)	2.27 (1)
σ^2 (O1)	0.016 (1)	0.018 (1)
α (%)	100.0	100.0
N (Mn-O2)	2	2
R_{eff} (Mn-O2)	2.37	2.37
R(Mn-O2)	2.57 (3)	2.55 (3)
σ^2 (O2)	0.012 (4)	0.015 (4)
α (%)	100.0	100.0
N (Mn-U1)	5	5
R_{eff} (Mn-U1)	3.87	3.87
R(Mn-U1)	3.78 (1)	3.78 (1)
σ^2 (U1)	0.011 (1)	0.013 (1)
α (%)	100.0	100.0
R-factor	0.0098	0.0071
Bond valence sum (O1)	1.56	1.62
Bond valence sum (O2)	0.24	0.26
Bond valence sum (total)	1.80	1.88

Table 2. Fitting parameters and results for 1200 ppm and 2400 ppm Mn-doped UO_2 oxide powders. (S_0^2) is the amplitude reduction factor, (ΔE_0) the shift from Mn K-edge position (5.989 keV), (N) the degeneracy, (R_{eff}) (Å) the reference bond length, (R) (Å) the fitted bond length, (σ^2) the Debye–Waller factor and (α) F-test factor. EXAFS data and fits are shown in Fig. 4

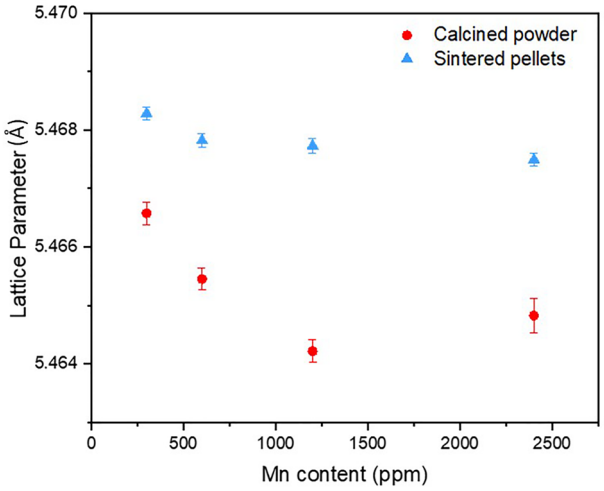

Figure 4. Lattice parameter values for calcined powder and sintered material, as determined by XRD. Errors are the standard deviation of triplicate analysis.

A charge balance mechanism is required in the substitution of Mn^{2+} on the U^{4+} site, provided by the formation of positive defects, U^{5+} and/or oxygen vacancies (O_v). Experimental evidence for U^{5+} formation can be determined using the High Energy Resolution Fluorescence Detected (HERFD) XANES method, with data acquired at the U M_4-edge; however, given that the doping level of Mn was low (300–2400 ppm), the amount of corresponding U^{5+} (up to 0.24%) is at, or below, the limits of detection of the technique. Nevertheless, principal component analysis of the data series revealed that, for the calcined powder, two components, attributed to U^{5+} (closely matching a standard of $CrUO_4$) and U^{4+} (UO_2) oxidation states, were required to accurately reconstruct each of the samples in the series (Fig. 5a and Supplementary Material Fig. 4).

Iterative target transformation factor analysis was used to indicate the approximate fraction of U^{4+} and U^{5+} in each of the oxide powders (Fig. 5b), with results indicating ~ 21–26 ± 2% U^{5+} present in Mn-doped UO_2 (and, therefore, ~ 74–79 ± 1% U^{4+}). Given the arguments above, the presence of U^{5+} seems unlikely to arise from a charge compensation mechanism, but from oxidation of the samples. Despite being exposed to air post-synthesis for the same period of time as the calcined samples, the sintered materials did not show any strong evidence for the presence of U^{5+} (Fig. 5c).

The formation of O_v defects was observed through Raman spectroscopy (Fig. 6a). The main T_{2g} peak (~ 445 cm^{-1}) of UO_2 and the defect band (~ 500–700 cm^{-1}), indicative of lattice distortion due to defect formation, was present for all samples. The relative intensity of individual peak contributions of the defect bands, where U1 is attributed to O_v, U2 to the LO phonon mode and U3 to O_i, was compared to the relative intensity of the T_{2g} peak[20] (Fig. 6b). There were minor fluctuations in the relative contributions as the concentration of Mn was increased; however, O_v were always found to be present (Fig. 6c), confirming their formation as a charge balance mechanism for Mn doping in UO_2.

As noted previously, there were no significant differences in the crystal structure of sintered Mn-UO_2 when compared to the calcined oxide powders, indicated by consistency in spectral features observed in the Mn K-edge XANES (Fig. 2) and the Fourier Transform of the EXAFS region (Fig. 3 and Supplementary Material Fig. 2). The reduction in UO_2 lattice parameter, due to Mn^{2+} substitution on the U^{4+} site, was maintained; although, the absolute values of lattice parameter were 0.002–0.004 Å greater in the sintered samples than the calcined samples (Fig. 4). This could be the result of volatilisation of Mn during sintering (see below) and/or reduction of U^{5+} (0.84 Å) to U^{4+} (1.00 Å) imposed by the reducing high temperature environment, as observed by HERFD-XANES (Fig. 5c), in which no U^{5+} was present.

Influence of reducing sintering conditions on the microstructure of Mn-doped UO_2.

When comparing the Mn concentrations of calcined oxide powders with those of materials sintered in a reducing (95% $N_{2(g)}$ / 5% $H_{2(g)}$) environment, it is evident that significant volatilisation of Mn occurred (Fig. 7a)[8]. For UO_2 doped with 300 ppm Mn, the loss was ~ 30%, while for the remaining concentrations (600, 1200 and 2400 ppm), it was ~ 80%.

No significant influence on the grain size was observed when the average measurements of ~ 500 grains were considered in comparison to undoped UO_2 (Fig. 7b–e); however, there was a marginal increase with increasing dopant concentration. An average grain size of 13.9–14.8 ± 0.5 µm was recorded, in comparison with undoped UO_2, sintered under the same conditions, which had an average grain size of 14.0 ± 0.2 µm. This is in contrast to previous studies[8] and modelling predictions[6], most likely due to the nature of the sintering atmosphere, which contained no O_2.

Studies of commercially available Cr-doped UO_2 have shown that the sintering atmosphere is the most important factor contributing to grain growth, with the addition of small quantities of oxygen thought to promote the formation of a 'CrO' eutectic phase. At sintering temperatures (> 1675 °C), this phase is liquid and aids grain growth, evidenced as precipitates of Cr_2O_3 formed upon cooling[21–24]. The effects of a eutectic phase have been

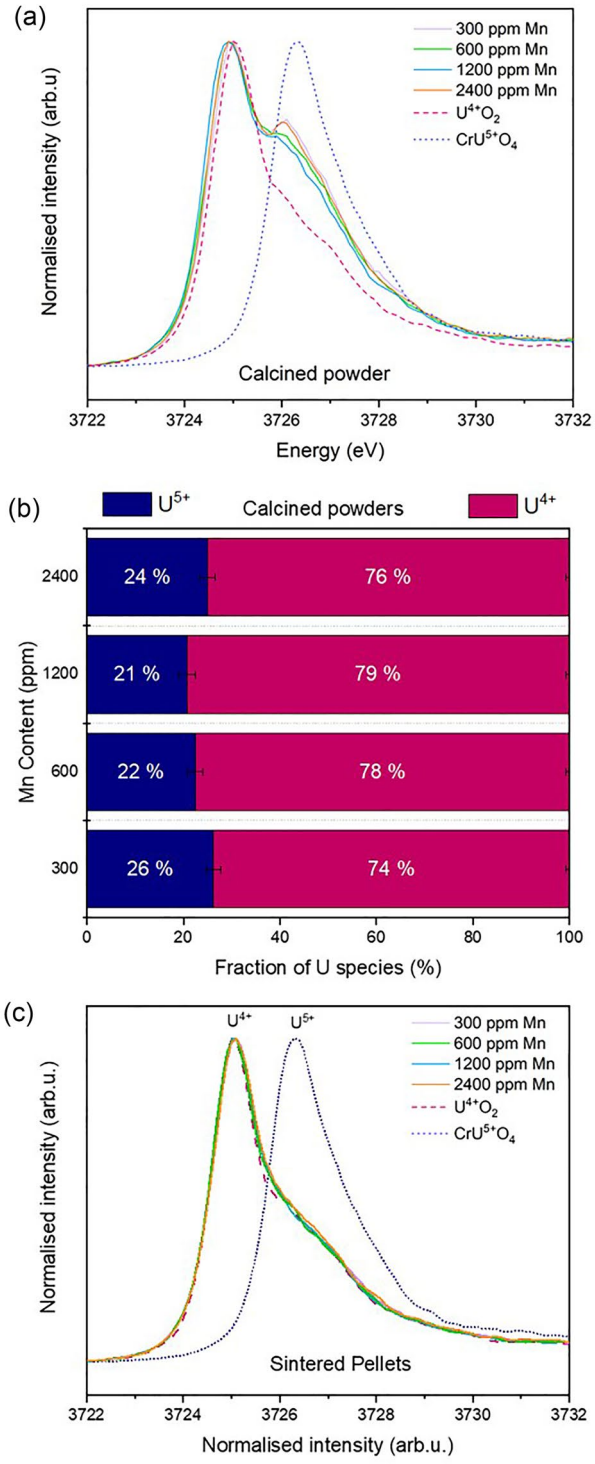

Figure 5. U M_4-edge HERFD XANES of Mn-doped UO_2 materials. (**a**) calcined material; (**b**) quantification of the $U^{4+/5+}$ ratio in calcined powder determined from fitting of U M_4-edge HERFD XANES data in (**a**); and (**c**) sintered material.

reported for Mn/Al doped UO_2 sintered in a H_2 atmosphere at 1860 °C, where a MnO/Al_2O_3 phase was observed by EDX mapping[10]. However, contrary to Cr-doped UO_2, the addition of oxygen to the sintering atmosphere in Mn/Al doped UO_2 resulted in a smaller grainsize, attributed to increased solubility of MnO in the UO_2 matrix[10].

In the present study, under fully reducing conditions, much of the Mn^{2+} incorporated into the UO_2 was volatilised, and no precipitates were observed, which indicates that the solubility limit of Mn in UO_2 was not reached and that an equivalent MnO liquid phase was not likely formed. Moreover, no significant increase in the grain

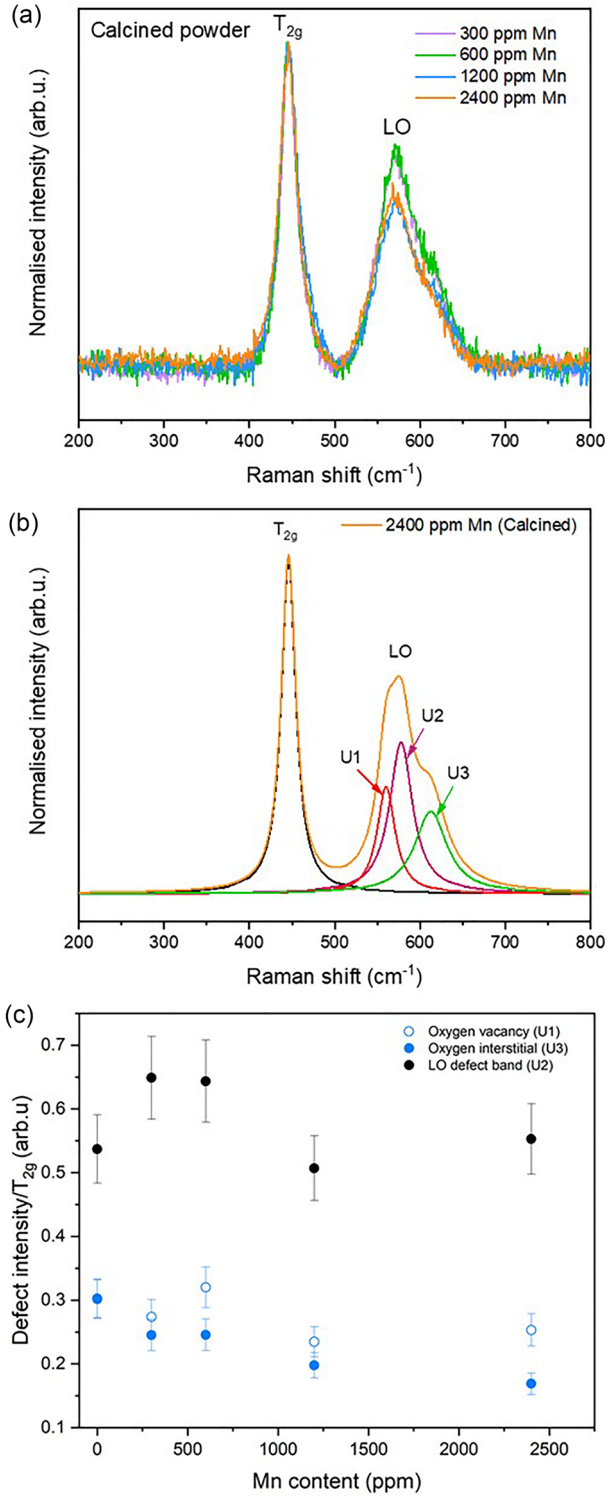

Figure 6. Raman analysis of Mn-doped UO_2 calcined powders. (**a**) Raman spectra; (**b**) deconvolution of the 2400 ppm Mn-doped UO_2 spectra into U1, U2 and U3 peaks; and (**c**) defect content realised by the area ratio of the defect peak to the T_{2g} peak.

growth was observed with increasing Mn concentration (Fig. 7). One reason for this is that the temperature of sintering (1700 °C) was below the melting point of MnO_2 (1945 °C), therefore, the formation of any possible eutectic phase was restricted. It has been previously shown, in Cr-doped UO_2, that, if the sintering atmosphere required for the eutectic phase formation is not met, the presence of precipitates at grain boundaries will have

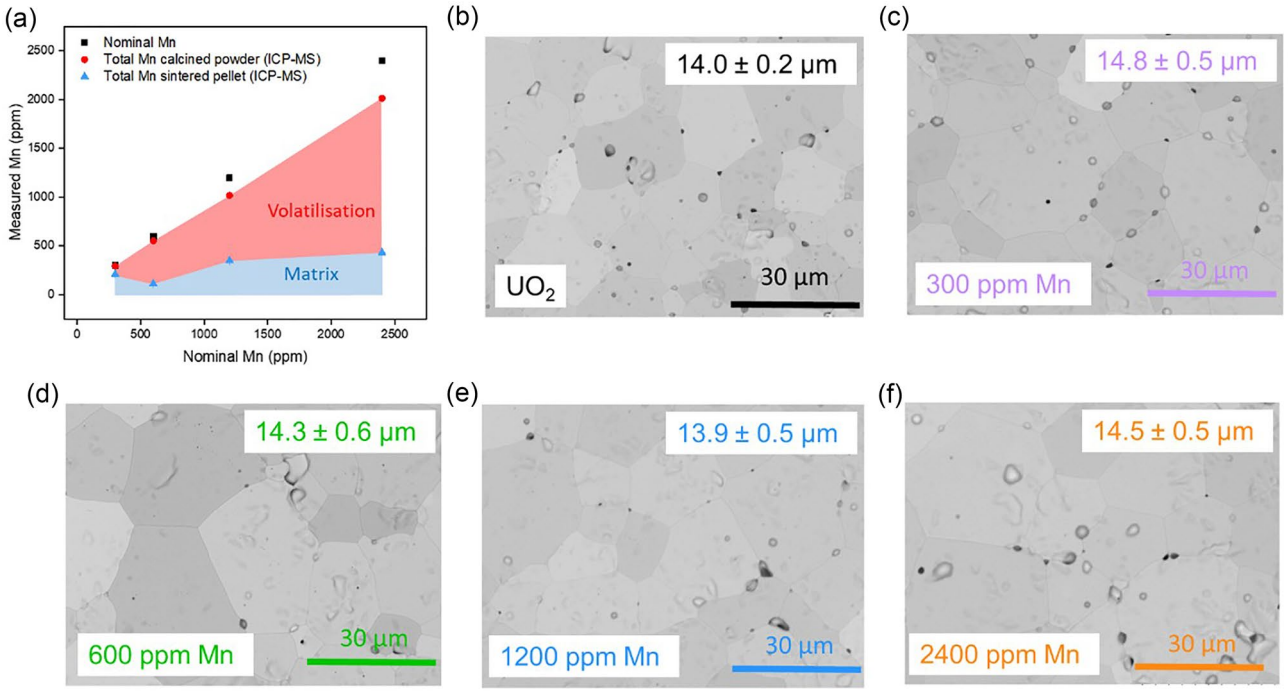

Figure 7. Microstructural evolution of undoped and Mn-doped UO_2 sintered in a reducing environment. (**a**) the measured Mn content in Mn-doped UO_2 calcined powder and sintered pellets; and SEM images and average grain size of ~ 500 grains measured across the sample surface in (**b**) undoped UO_2 and (**c**–**f**) Mn-doped UO_2 of increasing Mn content.

the opposite effect and grain growth will be hindered by grain boundary "pinning"[21]; however, this reasoning is excluded here due to the absence of precipitates in the Mn-doped UO_2 samples.

Despite the observation that the average grain size did not significantly increase upon increased levels of Mn doping, when compared with the undoped UO_2, individual grain sizes of up to 50 µm were observed for all Mn-doped UO_2 samples studied (Fig. 7b–e). This 'localised' grain growth has previously been reported for Mn-doped UO_2 prepared via sol–gel synthesis and sintered under reducing conditions (95% $Ar_{(g)}$ / 5% $H_{2(g)}$, 6h, 1700 °C)[8]. Such behaviour may be due to the increased diffusivity of U atoms predicted by atomistic models of the defect concentrations[7]. Further work to underpin the solubility limit of Mn in UO_2, and to develop an understanding of the influence of sintering conditions on Mn–UO_2, is required to fully elucidate the mechanism of grain size growth.

These results have given insight into the crystallographic basis for interpretation of grain growth as well as oxidation and dissolution behaviours in Mn-doped UO_2 and support development for future use as accident tolerant fuel.

Methods

Sample preparation

A wet synthesis method was developed using uranium nitrate hexahydrate ($UO_2(NO_3)_2{\cdot}6H_2O$, (The British Drug House (BDH). B.D.H Laboratory Chemicals Division, > 98%, 0.3 mol L^{-1}). This was mixed with manganese(II) nitrate tetrahydrate ($Mn(NO_3)_3{\cdot}4H_2O$, Sigma Aldrich, 99.99%, 1.6 mol L^{-1}) in the proportion required to give the desired concentration of dopant. An initial synthesis study was performed in which a number of samples were assessed to determine the optimal pH and calcination temperature for fabrication of Mn-doped UO_2. The final fabrication route is shown in Fig. 8 and is detailed as follows. Concentrated ammonium hydroxide, NH_4OH (5 mol L^{-1}), was added until a pH of 10 was reached. The resultant precipitate was vacuum filtered, washed in ultra-high quality (18 MΩ cm) water, and dried for 24 h at 90 °C. Thermogravimetric analysis was carried out on precursor material using a Netzsch TG 449 F3 Jupiter instrument coupled with a 64-channel QMS 403 D Aeolos mass spectrometer. Samples were heated to 1000 °C at a rate of 10 °C min^{-1} under a constant $Ar_{(g)}$ flow. Analysis of the mass loss over time determined that a calcination temperature of 750 °C for 4 h under a reducing (95% $N_{2(g)}$ / 5% $H_{2(g)}$) atmosphere was sufficient to convert the precursor material to oxide. Successful co-precipitation of Mn with U oxide was measured by inductively coupled plasma optical emission spectroscopy (ICP-OES) analysis of the supernatant, where > 99.9% precipitation was observed for both U and Mn for samples precipitated at pH 10.

Homogenised oxide powders, prepared via milling at 35 Hz for 15 min, were uniaxially pressed at 2.5 tonnes into 6 mm green pellets and sintered at 1700 °C for 8 h in a reducing atmosphere (95% $N_{2(g)}$ / 5% $H_{2(g)}$). Complete digest of precursor and calcined material, as well as sintered pellets (crushed to powder using a mortar and pestle), was carried out to assess the Mn content. In this method, 20 mg of sample was completely dissolved in 2M nitric acid (ultrapure HNO_3) at 90 °C, with the aid of a magnetic stirrer, and an aliquot was removed and analysed

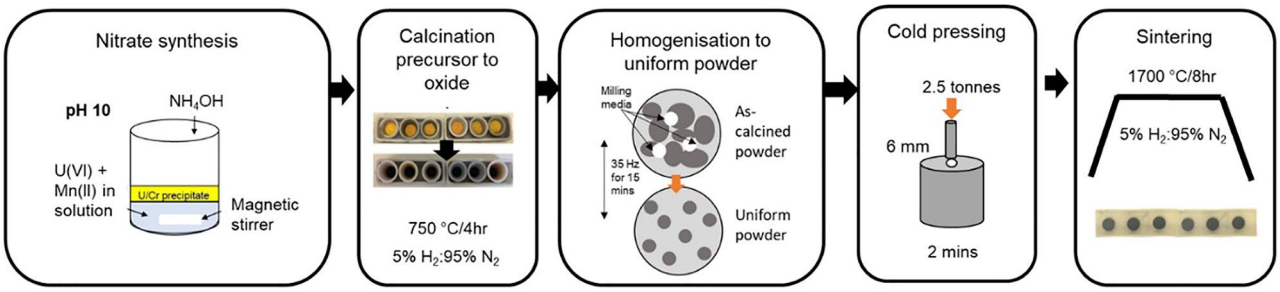

Figure 8. Optimised synthesis and fabrication route for Mn- doped UO_2.

by ICP-OES (Thermofisher Scientific iCAPDuo6300) for Mn and U concentration. Samples were dissolved in triplicate and an average measurement of Mn, with errors of 1 standard deviation, for each sample reported.

Characterisation

Secondary electron images of thermally etched pellet sample surfaces were taken using a Hitachi TM3030 scanning electron microscope at an accelerating voltage of 15 kV. Samples were thermally etched at 80–90% sintering temperature under a reducing atmosphere (95% $N_{2(g)}$ / 5% $H_{2(g)}$) and the revealed grains imaged at 500 × magnification. The Image J software was used to obtain the average grain size of ~ 500 grains in images taken from 5 different regions across the pellet surface.

A PANalytical Xpert3 diffractometer was used in reflection mode with a 45 keV/40 mA generator to characterise powder samples by XRD (XRD). Data were collected between 5° and 100° 2θ with a step size of 0.013° and a step time of 40 s, a fixed slit size of 0.5 was used. LaB_6 (20–30 wt%) was used as an internal standard for data alignment, corrected using the WinXPow software. Accurate determination of lattice parameters was carried out in the Topas software, using Le Bail refinements. To avoid oxidation, calcined powders were measured immediately post heat treatment (i.e. within 10 min of removal from the furnace) and sintered samples were crushed upon removal from the furnace, within a controlled inert atmosphere ($N_{2(g)}$), and immediately measured to avoid oxidation.

Mn K-edge (6.539 keV) and U M_4-edge (3.728 keV) X-ray Absorption Spectroscopy measurements were performed, at room temperature, on both calcined powder and sintered Mn-doped UO_2. The I20-scanning beamline at the Diamond Light Source (DLS), UK, was used in fluorescence mode to measure the Mn K-edge using a 64-element Ge detector with Xspress4 signal processing and a beam size of 400 × 300 μm (FWHM). A high flux and excellent energy resolution is given by the wiggler-sourced I20-scanning beamline due to the use of a Si(111) four-bounce crystal monochromator, allowing the detection of low concentrations of Mn dopant in the heavily absorbing UO_2 matrix.

Multiple scans were taken across a number of energy ranges to improve data quality. Energy steps of 5 eV were taken from 6439 to 6535 eV, 0.2 eV from 6536 to 6560 eV with a time step of 1 s $step^{-1}$ in the XANES region for all samples. In the EXAFS region for calcined Mn-doped UO_2 samples, an energy step of 0.04 $Å^{-1}$ was taken from 6560 – 6980 eV with a time step of 1–6 s $step^{-1}$. The spectral features in the sintered samples were identical to those of the calcined powers. A number of standards of known Mn valence state and coordination environment were measured in transmission mode, including a range of Mn^{2+} standards: $Mn^{2+}O$; $(Mn^{2+}, Fe)(Ta, Nb)_2O_6$; $Mn^{2+}SiO_6$; and $Mn^{2+}{}_2SiO_4$.

The E_0 (white line, taken from the peak of the first derivative) positions of the raw data were aligned to the E_0 position of a standardised reference Mn foil that was measured simultaneously with Mn-doped UO_2 samples. A cubic spline background subtraction and normalisation procedure[25] was then carried out and multiple scans merged using the Athena software[26]. To isolate the pre-edge region for analysis, an arctangent function was applied across the 6535.0–6548.0 eV energy range to remove the photoelectric background absorption[27] and three Gaussian peak functions used to model the pre-edge features (Supplementary Material Fig. 1). The energy position and normalised height were refined using the non-linear least-square fitting SOLVER function in Excel and the pre-edge centroid position assigned by taking the intensity weight average of each Gaussian fit.

To create models of the local environment realised in the EXAFS region, absorption data (eV) were converted to wavenumber, k ($Å^{-1}$), and a Fourier Transform of the resulting k space was used for fitting. The possible scattering paths of the Mn central absorber atom to the surrounding atoms in the Mn-doped UO_2 local environment were generated using a FEFF6 algorithm[28] in Artemis[26] where a UO_2 CIF file was modified to include Mn as the central absorbing atom at the first U lattice position. The range of k ($Å^{-1}$), r (Å), and the amplitude reduction factor ($S_0{}^2$) were optimised for the data and the following parameters allowed to refine: degeneracy (N); fitted bond length (R) (Å); shift from Mn K-edge position (6.539 keV) (ΔE_0) and; the Debye–Waller factor (σ^2). The F-test was applied to each fitted path, the result (α) indicated the confidence of adding the path to improve the fit (> 67% gives a confidence of 1σ, > 95% gives a confidence of 2σ)[29]. The bond valence sum (BVS) was calculated for the Mn–O coordination environment, which is an evaluation of bond distances in a coordination shell that are equal to the formal oxidation state of the cation absorber[30].

HERFD XANES was carried out at the U M_4-edge using the BM20 beamline at the European Synchrotron (ESRF), France[31], with the use of an X-ray emission spectrometer[32]. Calcined powders were mixed with polyethylene glycol (PEG) and pressed into 6 mm pellets for analysis, while the as-sintered surfaces of pellets were

measured. Raw U M_4-edge data was pre-processed in Athena, as discussed above, and a principal component analysis was used to determine the possible number of spectral components, followed by Iterative Target Transformation Factor Analysis (ITTFA)[33] to indicate the relative concentration of each component using $U^{(4+)}O_2$ and $CrU^{(5+)}O_4$ standards measured alongside Mn-doped UO_2 at the BM20 beamline.

Raman measurements were performed using a Renishaw inVia Reflex confocal spectrometer equipped with a Leica DM2500 microscope. Calcined Mn-doped UO_2 powders were pressed into pellets before analysis using a 514.5 nm green argon laser with 1800 lines mm^{-1} grating to acquire a spectral acquisition between 200 and 800 cm^{-1}. An average of 10 points across the compacted green pellet surface of each pellet was taken, to confirm their reproducibility and homogeneity of the composition across the sample. Lorentz function fitting was used to obtain information of peaks attributed to defects (U1, U2 and U3) in the UO_2 structure, relative to the main T_{2g} band of UO_2 at 445 cm^{-1}. In addition to the U2 LO phonon band at ~ 574 cm^{-1}, the U1 peak at ~ 527 cm^{-1} attributed to O_v defects, and U3 peak at ~ 634 cm^{-1} attributed to O_i defects, were identified[19].

Data availability

The data that support the findings of this study are available from the corresponding author, upon reasonable request.

Received: 18 August 2023; Accepted: 22 December 2023
Published online: 18 January 2024

References

1. Arborelius, J. *et al.* Advanced doped UO_2 pellets in LWR applications. *J. Nucl. Sci. Technol.* **43**, 967–976 (2006).
2. Massih, A. Effects of additives on uranium dioxide fuel behaviour, *Swedish Radiat. Saf. Auth.* 74 (2014).
3. Killeen, J. C. Fission gas release and swelling in UO_2 doped with Cr_2O_3. *J. Nucl. Mater.* **88**, 177–184 (1980).
4. Kashibe, S. & Une, K. Effect of additives (Cr_2O_3, Al_2O_3, SiO_2, MgO) on diffusional release of ^{133}Xe from UO_2 fuels. *J. Nucl. Mater.* **254**, 234–242 (1998).
5. Une, K., Tanabe, I. & Oguma, M. Effects of additives and the oxygen potential on the fission gas diffusion in UO_2 Fuel. *J. Nucl. Mater.* **150**, 93–99 (1987).
6. Cooper, M. W. D., Andersson, A. D. R. & Stanek, C. R. *Mn-Doped Oxide Nuclear Fuel*, United States Patent, US 10,847,271 B1 (2020).
7. Cooper, M. W. D., Stanek, C. R. & Andersson, A. D. R. The role of dopant charge state on defect chemistry and grain growth of doped UO_2. *Acta Mater.* **150**, 403–413 (2018).
8. Finkeldei, S. C. *et al. Synthesis and characterization of UO_2 feedstocks containing controlled dopants.* Oak Ridge National Laboratory Report, ORNL/SPR-2019/1067 (2019).
9. Kang, K. W. *et al.* Effects of MnO–Al_2O_3 on the grain growth and high-temperature deformation strain of UO_2 fuel pellets. *J. Nucl. Sci. Technol.* **47**, 304–307 (2010).
10. Ewing, R. C. Long-term storage of spent nuclear fuel. *Nat. Mater.* **14**, 252–257 (2015).
11. Nuclear Decommissioning Authority. *Geological Disposal: Package Evaluation Status Report*, NDA Report no. SCCS/451/01 (2016).
12. Smith, H. *et al.* Oxidative dissolution of Cr-doped UO_2 nuclear fuel. *npj Mater. Degrad.* **7**, 25 (2023).
13. Martinez, J. *et al.* From uranium(IV) oxalate to sintered UO_2: Consequences of the powders thermal history on the microstructure. *J. Eur. Ceram. Soc.* **35**, 4535–4546 (2015).
14. De Bruijn, T. J. W., De Ruiter, G. M. J., De Jong, W. A. & Van Den Berg, P. J. Thermal decomposition of aqueous manganese nitrate solutions and anhydrous manganese nitrate. Part 2. Heats of reaction. *Thermochim. Acta* **45**, 279–292 (1981).
15. Rajagopalan, K. V., Ravindran, P. V. & Radhakrishnan, T. P. Thermal Decomposition of uranyl nitrate hexhydrate: A thermal analysis - mass spectrometry study. *J. Therm. Anal.* **44**, 89–96 (1995).
16. Farges, F. *Ab initio* and experimental pre-edge investigations of the Mn K -edge XANES in oxide-type materials. *Phys. Rev. B* **71**, 155109 (2005).
17. Chalmin, E., Farges, F. & Brown, G. E. A pre-edge analysis of Mn K-edge XANES spectra to help determine the speciation of manganese in minerals and glasses. *Contrib. Mineral. Petrol.* **157**, 111–126 (2009).
18. Dräger, G., Kirchner, T., Bocharov, S. & Kao, C. C. Spin-resolved NEXAFS from resonant X-ray scattering. *Int. Union Crystallogr.* **8**, 398–400 (2001).
19. Smith, H. *et al.* Cr^{2+} solid solution in UO_2 evidenced by advanced spectroscopy. *Comm. Chem.* **5**, 163 (2022).
20. Guimbretière, G. *et al.* Determination of in-depth damaged profile by Raman line scan in a pre-cut He^{2+} irradiated UO_2. *Appl. Phys. Lett.* **100**, 251914 (2012).
21. Bourgeois, L., Dehaudt, P., Lemaignan, C. & Hammou, A. Factors governing microstructure development of Cr_2O_3-doped UO_2 during sintering. *J. Nucl. Mater.* **297**, 313–326 (2001).
22. Kuri, G. *et al.* Local atomic structure of chromium bearing precipitates in chromia doped uranium dioxide investigated by combined micro-beam X-ray diffraction and absorption spectroscopy. *J. Nucl. Mater.* **449**, 158–167 (2014).
23. Leenaers, A., De Tollenaere, L., Delafoy, C. & Van den Berghe, S. On the solubility of chromium sesquioxide in uranium dioxide fuel. *J. Nucl. Mater.* **317**, 62–68 (2003).
24. Cardinaels, T. *et al.* Chromia doped UO_2 fuel: Investigation of the lattice parameter. *J. Nucl. Mater.* **424**, 252–260 (2012).
25. Newville, M. IFEFFIT: Interactive XAFS analysis and FEFF fitting. *J. Synchrotron Radiat.* **8**, 322–324 (2001).
26. Ravel, B. & Newville, M. ATHENA, ARTEMIS, HEPHAESTUS: Data analysis for X-ray absorption spectroscopy using IFEFFIT. *J. Synchrotron Radiat.* **12**, 537–541 (2005).
27. Waychunas, G. A. Synchrotron radiation XANES spectroscopy of Ti in minerals: Effects of Ti bonding distances, Ti valence, and site geometry on absorption edge structure. *Am. Mineral.* **72**, 89–101 (1987).
28. Ankudinov, A. & Ravel, B. Real-space multiple-scattering calculation and interpretation of X-ray absorption near-edge structure. *Phys. Rev. B Condens. Matter Mater. Phys.* **58**, 7565–7576 (1998).
29. Downward, L., Booth, C. H., Lukens, W. W. & Bridges, F. A variation of the F-test for determining statistical relevance of particular parameters in EXAFS fits. *AIP Conf. Proc.* **882**, 129–131 (2007).
30. Brown, I. D. & Altermatt, D. Bond-valence parameters obtained from a systematic analysis of the inorganic crystal structure database. *Acta Crystallogr. Sect. B.* **41**, 244–247 (1985).
31. Scheinost, A. C. *et al.* ROBL-II at ESRF: A synchrotron toolbox for actinide research. *J. Synchrotron Radiat.* **28**, 333–349 (2021).
32. Kvashnina, K. O. & Scheinost, A. C. A Johann-type X-ray emission spectrometer at the Rossendorf beamline beamlines. *J. Synchrotron Radiat.* **23**, 836–841 (2016).
33. Rossberg, A. *et al.* Identification of uranyl surface complexes on ferrihydrite: Advanced EXAFS data analysis and CD-music modeling. *Environ. Sci. Technol.* **43**, 1400–1406 (2009).

34. Hyatt, N. C. *et al.* The HADES facility for high activity decommissioning engineering & science: Part of the UK national nuclear user facility. *IOP Conf. Ser. Mater. Sci. Eng.* **818**, 012022 (2020).

Acknowledgements
This work was funded by the UK Engineering and Physical Science Research Council (EPSRC) under Grant Numbers EP/N017374/1, EP/S020659/1 and EP/L015390/1. This research utilised the HADES/MIDAS facility[34] at the University of Sheffield established with financial support from EPSRC and BEIS (Grant Number EP/T011424/1) and also the PLEIADES National Nuclear User Facility, established with funding from EPSRC (Grant Number EP/V035215/1). We acknowledge Diamond Light Source for time on I20-scanning under proposal number SP28515. We acknowledge the European Synchrotron Radiation Facility for provision of synchrotron radiation facilities (under proposal number MA-4821) and we would like to thank Tatiana Poliakova, Anastasiia Smirnova and Jurij Galanzew for assistance in using the Rossendorf beamline (ROBL, BM20) remotely during the pandemic. The authors also wish acknowledge Sarah Pepper, Daniel Austin and Daniel Bailey for help with the ICP-OES, X-ray absorption spectroscopy analysis and Thermogravimetric analysis, respectively.

Author contributions
H.S. – data collection, formal analysis, original draft preparation. L.T. – formal analysis, original draft preparation, reviewing and editing. R.M. data collection, formal analysis, original draft preparation, reviewing and editing. M.S. - data collection, formal analysis. K.K. – data collection, formal analysis, reviewing and editing. F.M. – data collection, reviewing and editing. N.H. – data collection, reviewing and editing. C.C. – funding acquisition, supervision, data collection, formal analysis, reviewing and editing.

Competing Interests
The authors declare no competing interests.

Additional information
Supplementary Information The online version contains supplementary material available at https://doi.org/10.1038/s41598-023-50676-2.

Correspondence and requests for materials should be addressed to C.L.C.